*Exploration Geophysics (2004) **35**, 19–24*
Butsuri-Tansa (Vol. 57, No. 1)
Mulli-Tamsa (Vol. 7, No. 1)

Seismic waveform tomography in the frequency-space domain: selection of the optimal temporal frequency for inversion

Toshiyuki Yokota[1] Jun Matsushima[2]

Key Words: waveform tomography, frequency-space domain, optimal temporal frequency selection

ABSTRACT

Frequency-space domain full-wave tomography is a promising technique for delineating detailed subsurface structure with high resolution. However, this method requires criteria for the selection of a set of optimal temporal frequency components, to achieve stability in the sequence of inversion processes together with computational efficiency. We propose a method of selecting optimal temporal frequencies, based on wavenumber continuity. The proposed method is tested numerically and is shown to be able to select an optimal set of frequency components that are sufficient to image the anomalies.

INTRODUCTION

Recently, there has been a considerable amount of research on seismic tomography (Harris et al., 1995; Wong, 2000), and traveltime tomography has been developed as a practical technology applicable to exploration and exploitation in real environments. Traveltime tomography has already been successfully used to monitor fluid movement during steam-injection or heat-stimulation enhanced oil recovery (Mathisen et al., 1995). Lazaratos and Marion (1997) also described a case in which seismic tomography was used successfully to monitor CO_2 gas injection, obtaining results with a resolution of about 3 m using an inversion technique with a laterally-varying thin layer model. Such high resolution satisfies the needs of reservoir engineers.

Traveltime tomography is an important and valuable method because it is robust and computationally efficient. These merits are realized through ray theory that assumes a seismic wave with infinite frequency. However, the resolution of ray tomography is severely limited because ray theory neglects the existence of scattering, and reduces the information contained in a seismic trace to one traveltime pick. Some researchers have concluded that the minimum feature size resolvable by ray tomography is of the order of the width of the first Fresnel zone (Willamson, 1991; Williamson and Worthington, 1993; Shuster, 1995).

Full-wave tomography has been developed recently (Tarantola, 1984; Tarantola, 1986; Pratt and Worthington, 1990), and formulation in the time-space domain (Tarantola, 1984) was developed in advance of formulation in the frequency-space domain (Pratt and Worthington, 1990). The technique primarily aims to improve models iteratively by back-propagating the data residuals and correlating the result with forward-propagated wavefields in a manner similar to prestack reverse-time migration. In comparison to traveltime tomography, full-wave tomography has the capacity for achieving higher resolution, and for including many kinds of subsurface physical properties such as S-wave velocity, density, and Q values. However, the method is computationally intensive, requiring much larger computational power and longer time.

Generally, wave equation modelling in the time-space domain is more popular than in the frequency domain, because of the ease of implementation and lesser requirements for computational memory. However, if the modelling is intended for seismic exploration purposes, frequency-domain modelling is more practical from the standpoint of computational cost, because multi-source data acquisition can be simulated rapidly by using direct multiplication (back substitution) once the triangular factors of the impedance matrix have been calculated. Furthermore, under sufficient conditions of spectral coverage, inversions can be performed with only a few temporal frequency components (Pratt and Worthington, 1990; Pratt, 1999). Note that inversion using all frequencies is equivalent to time-domain waveform inversion.

In contrast to the case of time-domain inversion that theoretically requires all frequencies at once, a limited number of frequencies is sufficient for a reasonably stable and accurate inversion in the frequency domain (Pratt, 1999). However, the problem of selection of appropriate frequencies for inversion becomes significant. Too few frequency components will result in an unstable inversion or possibly a local minimum, whereas too many frequencies will simply increase redundancy and waste computer resources and time. Therefore, there should be an optimal set of frequencies that satisfies both stability and efficiency of inversion.

We have developed a methodology for determining the optimal temporal frequency sequence for inversion. There are several factors to be considered, including the scale of observation, the size of anomalies, and the velocity range. Under conditions of weak scattering, these factors can be rearranged into a relationship between frequency in the time domain and wavenumber in the space domain. The maximum wavenumber is determined by the resolution of the inversion. On the other hand, the minimum wavenumber is defined by the maximum phase error. We conclude, through numerical experiments in this study, that full wavenumber coverage is necessary to extract information on velocity models using a minimal set of frequency components of the data.

METHODOLOGY

We have selected the frequency-domain finite-difference method the forward modelling and inversion method in this study, despite the time-domain approach being more popular and easier in implementation. The reasons for this choice are that, in contrast to the time-domain method, which essentially requires all frequencies simultaneously, stable inversion in the frequency domain can be performed with only a few temporal frequency components.

[1] *National Institute of Advanced Industrial Science and Technology, 1-1-1-C7 Higashi, Tsukuba 305-8567, JAPAN*
Tel: +81-29-861-2464
Fax: +81-29-861-3618
Email: yokota-t@aist.go.jp

[2] *Japan National Oil Corp., Technology Research Center, 1-1-1-C7 Higashi, Tsukuba 305-8567, JAPAN*

Manuscript received July 14, 2003; accepted September 3, 2003. Part of this paper was presented at the 6th SEGJ International Symposium (2003).

Full-wave tomography (waveform inversion)

As a brief review of the implementation of waveform inversion, we begin with the acoustic wave equation in the time domain, ignoring energy sources for simplicity:

$$\frac{\partial^2 p(x,t)}{\partial t^2} = K \frac{\partial}{\partial x_i}\left[\frac{1}{\rho}\frac{\partial p(x,t)}{\partial x_i}\right], \quad (1)$$

where x is an arbitrary spatial axis, p is the pressure as a function of time and position, K is the bulk modulus, and ρ is the bulk density. Note that the right-hand side of equation (1) implies spatial summation over the range of i. After applying the Fourier transform to equation (1), we obtain the acoustic wave equation in the frequency domain:

$$-\omega^2 P(x,\omega) = K \frac{\partial}{\partial x_i}\left[\frac{1}{\rho}\frac{\partial P(x,\omega)}{\partial x_i}\right], \quad (2)$$

where ω is the angular frequency and $P(x,\omega)$ is the Fourier spectrum of the pressure field at position x. By introducing the source term under a constant density condition, we obtain

$$\nabla^2 P(x,\omega;x_s) + \frac{\omega^2}{v(x)^2} P(x,\omega;x_s) = -S(\omega;x_s), \quad (3)$$

where $v(x)$ is the wave velocity and $S(\omega;x_s)$ is the Fourier spectrum of the source pressure when the source is located at position x_s. For simplicity, equation (3) is rewritten as

$$\mathbf{F}\,\mathbf{P} = -\mathbf{S}, \text{ or} \quad (4a)$$

$$\mathbf{P} = -\mathbf{F}^{-1}\,\mathbf{S}, \quad (4b)$$

where the complex impedance matrix $\mathbf{F}$ is a function of the angular frequency and of the velocity field. $\mathbf{P}$ and $\mathbf{S}$ are the Fourier spectra of the pressure field and the source term, respectively. Equation (4b) is representational, as it is not practical (or nearly impossible) to calculate the inverse of the huge impedance matrix $\mathbf{F}$. The implicit finite-difference method is therefore employed to solve equation (4a), using direct matrix factorization methods. In this study, we use a 25-point finite-difference operator (Shin and Sohn, 1998) to build the large and sparse impedance matrix $\mathbf{F}$, and an LU decomposition scheme is used to solve equation (4a). The matrix $\mathbf{F}$ is independent of the source term, and depends only on the elastic parameters and frequency. Therefore, once the matrix has been computed, it can be used to solve the pressure distribution for other additional sources with minimal additional computational cost, in contrast to calculation in the time-domain, the computational complexity of which is proportional to the number of sources.

For a multi-source problem with M sources, the residual error at the N receiver node points, $\delta\mathbf{P}$, is defined as the difference between the current model response ($\mathbf{P}_{calc}$), calculated by forward modelling, and the observed data ($\mathbf{P}_{obs}$) at each receiver location in the inversion process. Thus,

$$\delta\mathbf{P} = \mathbf{P}_{obs} - \mathbf{P}_{calc} \quad (5a)$$

or

$$\delta P_i^k = P_{obs\,i}^{\ k} - P_{calc\,i}^{\ k} \;;\; k = (1,2,...,M),\ i = (1,2,...,N), \quad (5b)$$

where the superscript k and subscript i represent the source and receiver number, respectively. In the process of least-squares fitting, the L_2 norm of the data residual errors $E(\mathbf{v})$ is minimised:

$$E(\mathbf{v}) = \frac{1}{2}\delta\mathbf{P}^t\delta\mathbf{P}^* \quad (6)$$

where $\mathbf{v}$ is the vector description of the current velocity model, the superscript t represents the matrix transposition, and the superscript * represents the complex conjugate.

The Newton method is adopted for inversion, derived by a Taylor-series expansion of the misfit function $E(\mathbf{v})$ of equation (6) in the vicinity of the current velocity model ($\mathbf{v}$) as

$$\begin{aligned} E(\mathbf{v}+\delta\mathbf{v}) &= E(\mathbf{v}) + \delta\mathbf{v}^t\frac{\partial E(\mathbf{v})}{\partial \mathbf{v}} + \frac{1}{2}\delta\mathbf{v}^t\frac{\partial^2 E(\mathbf{v})}{\partial \mathbf{v}^2}\delta\mathbf{v} + O\left(\|\delta\mathbf{v}\|^3\right) \\ &= E(\mathbf{v}) + \delta\mathbf{v}^t\nabla_{\mathbf{v}}E(\mathbf{v}) + \frac{1}{2}\delta\mathbf{v}^t\mathbf{H}\delta\mathbf{v} + O\left(\|\delta\mathbf{v}\|^3\right) \end{aligned} \quad (7)$$

where $\nabla_{\mathbf{v}}$ is the gradient (first derivative) function and $\mathbf{H}$ is the Hessian (second derivative) function of the error function E. To obtain the vector $\delta\mathbf{v}$ that minimises the misfit function, we differentiate $E(\mathbf{v} + \delta\mathbf{v})$ with respect to each of the model perturbations in $\delta\mathbf{v}$, and set each result to zero (neglecting higher order terms), with the result

$$\mathbf{H}\delta\mathbf{v} = -\nabla_{\mathbf{v}}E. \quad (8)$$

See Pratt et al. (1998) for more details.

Spectral coverage

Before discussing frequency selection in the inversion procedure for full-wave tomography, we also review the theory of diffraction tomography. Assuming crosswell acquisition geometry, it is possible to identify the areas of spectral coverage, as shown in Figure 1, using single frequency components under weak scattering and dense spatial sampling conditions (Devaney, 1984; Wu and Toksöz, 1987; Pratt and Worthington, 1990).

Figures 1a and 1b illustrate the coverage for low and high frequency components. Figure 1 basically shows the close relationship between frequency and resolution. The spectral coverage at higher frequency contains a larger number of wavenumber components, or in other words, the higher frequency component has the potential to resolve smaller-scale structures.

Figure 1 also demonstrates some other important features, such as the limited spectral coverage at low k_z. This phenomenon corresponds to the well-known fact that the crosswell geometry is insensitive to vertical structures. On the other hand, maximum

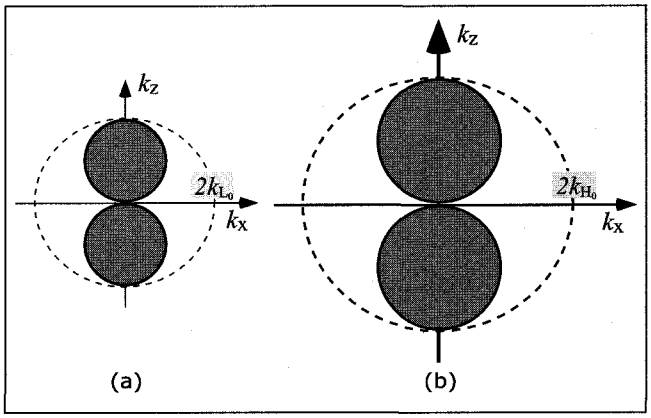

Fig. 1. Spectral coverage of (a) low frequency case and (b) high frequency case, respectively.

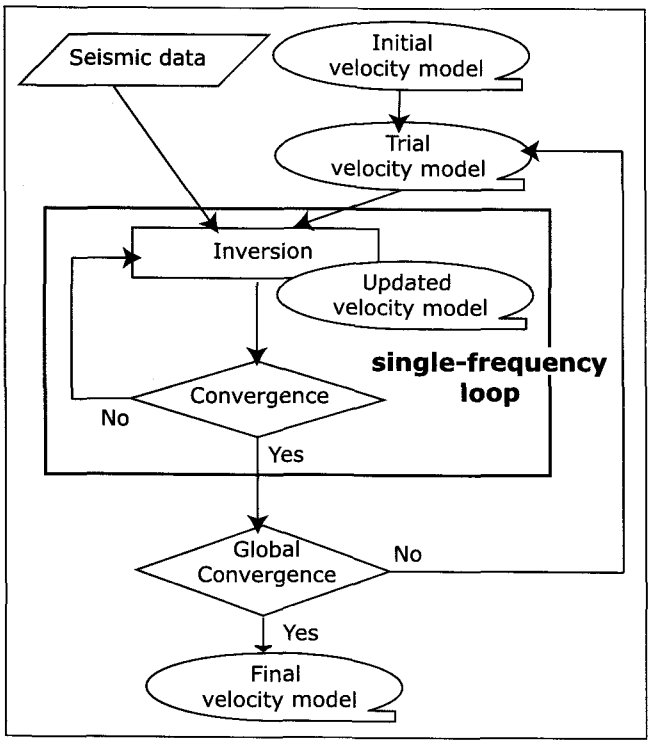

Fig. 2. Flowchart of the "consecutively ordered single-frequency inversion".

coverage is anticipated at low k_x, illustrating that the crosswell geometry is very suitable for detecting horizontal structures.

Consecutively ordered single-frequency inversion

In the procedure for frequency-space domain full-wave tomography, specific frequencies can be selected arbitrarily. From the viewpoint of computation efficiency, a consecutively ordered single-frequency inversion is adopted. The single-frequency inversion is analogous to obtaining the response of a single-frequency oscillator in the time-space domain. As indicated in the flowchart shown in Figure 2, the method uses a double-loop algorithm with a constant frequency component inside the inner small loop. It is important to start the inversion at sufficiently low frequency and low spatial wavenumber components, to maximise the chance of locating the global minimum. Calculations are iterated until the inversion evaluation function becomes smaller than the threshold. We use the normalized misfit function, averaged over the chosen frequencies, for the inversion evaluation function (E_{ave}), i.e.,

$$E_{ave} = \frac{1}{2 \cdot N_{freq}} \int_f \frac{\delta P(f)^t \delta P(f)^*}{\left| P(f)^t P(f)^* \right|}, \qquad (9)$$

where N_{freq} is the number of frequencies used to calculate the evaluation function. The denominator of the integrand represents the least-squares average of the observed data. After each single-frequency loop, the frequency is increased for the next loop to ensure inversion stability. Iterative calculation is continued until the inversion is converges globally.

Temporal frequency selection

Coarser frequency sampling improves inversion efficiency. On the other hand, for inversion stability, the frequency components used in the inversion are required to satisfy the weak scattering conditions. In the present paper, the trade-off condition is satisfied by an approach that maintains continuity of scale of the geological structures to be determined by the inversion.

After the inner small loop, using an arbitrary frequency component in the process of consecutively ordered single-frequency inversion, geological structures whose scale corresponds to that of a certain range of wavenumbers ($k_{min} \le k \le k_{max}$) can be inverted. The maximum wavenumber (k_{max}) can be determined by the resolution of the inversion because larger wavenumbers correspond to smaller geological structures, under constant-velocity conditions. The minimum value (k_{min}) is closely related to inversion stability, and can be determined with respect to individual frequency components to avoid cycle skipping. We determine the maximum and minimum wavenumbers in the following way.

First, we determine the maximum wavenumber, which is closely related to the minimum resolvable size of the geological structure. We define the upper limit of the wavenumber using the ray tomography result introduced by Williamson (1991) and Williamson and Worthington (1993), i.e.,

$$k_{max} = \sqrt{\frac{4\pi f}{LV}} \qquad (10)$$

where L is the ray-path length, f is the selected frequency, and V is the background velocity. Although resolution estimated on the basis of traveltime tomography could be lower than that achievable by full-waveform tomography, the approach is appropriate in this case, because the purpose of this calculation is simply to determine the maximum spatial frequency as a parameter for calculations of wavenumber continuity and trade-off between efficiency and stability of inversion.

We now consider the minimum wavenumber (k_{min}), which controls inversion stability. The weak scattering assumption, which assures stable inversion, is only valid when the difference between the true and current model is sufficiently small. The stability of inversion decreases rapidly as the difference between models increases, because of cycle skipping. Such instability occurs more easily at higher frequencies. This can be easily understood in the time-space domain, as shown in Figure 3. When carrying out frequency-space domain waveform inversion, minimisation of the phase error corresponds to the minimisation of the traveltime error in the time-space domain. For the case of low, single-frequency inversion (Figure 3a), traveltimes can be updated in the correct direction. In contrast, the possibility arises that modification will be in the wrong direction when high-frequency components are used (Figure 3b). Cycle skipping occurs when the phase difference between the true (observed) wave and the calculated (forward model) wave is larger than $\lambda/2$. The high-frequency component is therefore more prone to failure for a given traveltime error.

When conducting single-frequency inversion, the optimal frequency for the next outer-loop iteration is determined by the wavenumber component used for the present iteration, and the maximum phase error that can avoid cycle skipping. This condition is written as:

$$\frac{\Delta\varphi_{max}(f)}{2\pi} \cdot \frac{L}{k_{max}^{f_{current}}} \le \frac{\lambda(f)}{2}, \qquad (11)$$

where $\Delta\varphi_{max}(f)$ is the maximum phase error estimated for each frequency using the updated model after a single-frequency loop, $k_{max}^{f_{current}}$ is the maximum wavenumber for the current frequency, and $\lambda(f)$ is the wavelength corresponding to the current frequency.

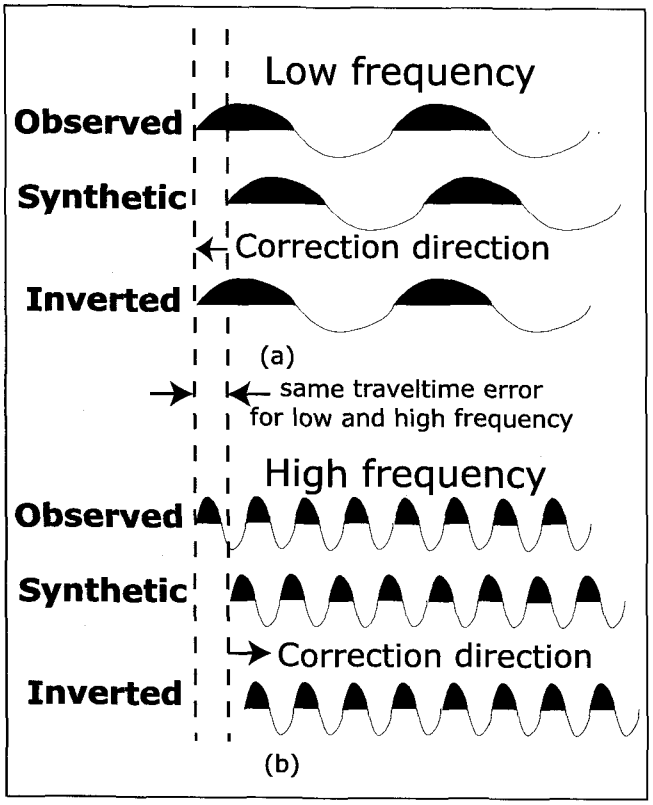

Fig. 3. Schematic illustration of cycle skipping with a monochromatic wavelet in the time domain: (a) Low-frequency monochromatic wavelet without cycle skipping. (b) High-frequency and cycle-skipped monochromatic wavelet. Though the traveltime error is the same for both cases, cycle skipping occurs only for the higher frequency.

Equation (11) can be rearranged as

$$f_{\text{next}} \le \frac{\pi V}{\Delta\varphi_{\max}(f)\cdot L}\cdot k_{\max}^{f_{\text{current}}}, \qquad (12)$$

where V is the background velocity and fnext is the optimal frequency for the next single-frequency loop, derived by this method.

The process for determining the frequency components as inputs for inversion is illustrated in Figure 4, and involves:

(1) Initiating inversion with a sufficiently low frequency (f_1).
(2) Determining the maximum spatial wavenumber ($k_{\max}^{f_1}$) for the chosen f_1 by choosing the limit of resolution in ray tomography with equation (10).
(3) Considering the maximum phase error in the inversion process, and the continuity of the spatial wavenumber, the optimal frequency (f_2) for the next iteration is calculated with equation (12), to satisfy the condition that $k_{\max}^{f_1}$ is equal to the minimum spatial wavenumber for the next iteration ($k_{\min}^{f_2}$).
(4) Steps (2) and (3) are repeated iteratively.

NUMERICAL EXPERIMENT

We conducted a numerical experiment to examine the validity of the proposed method. The two-dimensional model shown in Figure 5 was used for the numerical experiment. It contains three circular high-velocity anomalies within the background velocity of 3000 m/s.

The diameters of the three circular anomalies were 3, 11, and 33 m, with velocities of 3200, 3100, and 3050 m/s. The diameter

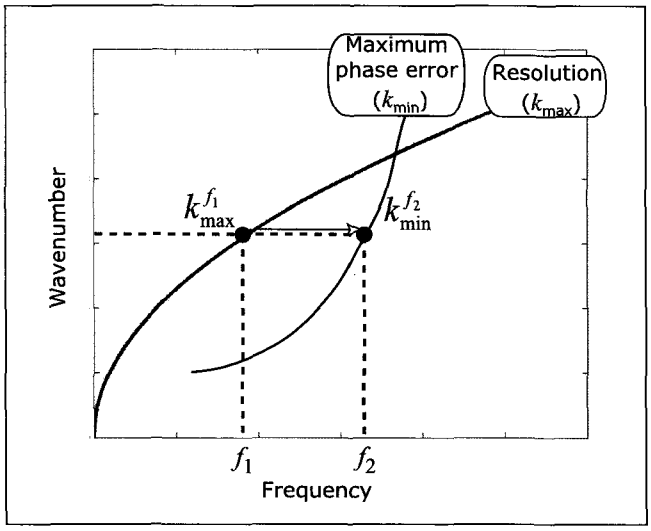

Fig. 4. Procedure for optimal frequency selection.

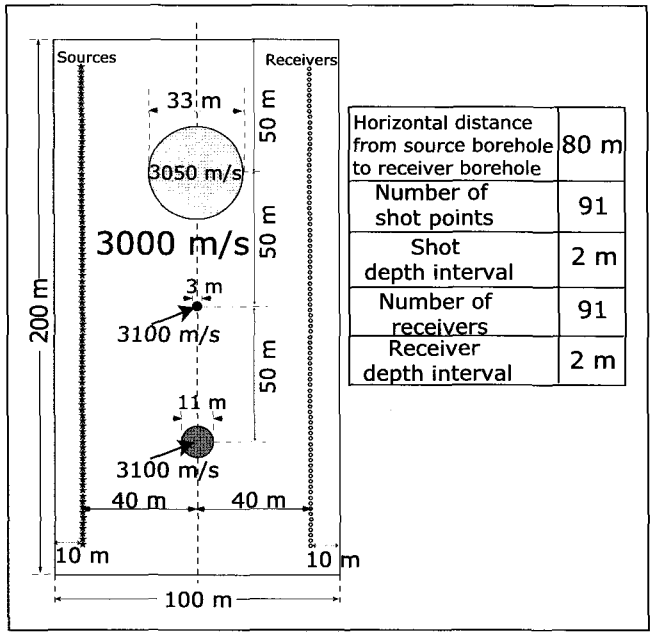

Fig. 5. Model used for the numerical experiment.

of the maximum anomaly was approximately the same as the seismic wavelength at 100 Hz (30 m). The size of the model was 100 m in the horizontal direction and 200 m vertically. Shot points were located vertically 10 m apart from the left edge of the model, with 2-m depth intervals. Receivers were located vertically 10 m from the right edge, with 2-m depth intervals. The horizontal distance from the shot array to the receiver array was 80 m.

We simulated the observed dataset by two-dimensional acoustic modelling in the time-space domain. The wave field was calculated by a pseudo-spectral method (Murayama et al., 1991; Furumura et al., 1998) using an isotropic source, with a Ricker wavelet of central frequency 100 Hz. The sampling interval was 1 ms, and the waveform data consisted of 1024 samples. We then used the Fourier-transformed spectrum of the waveform as the input for inversion in the frequency-space domain. The inversion model was composed of square cells with 1-m side lengths.

Figure 6 illustrates the process within a single-frequency loop of the consecutively ordered single-frequency inversion, at a temporal frequency of 150 Hz. The initial velocity model for this frequency loop comes from the inversion result of the previous

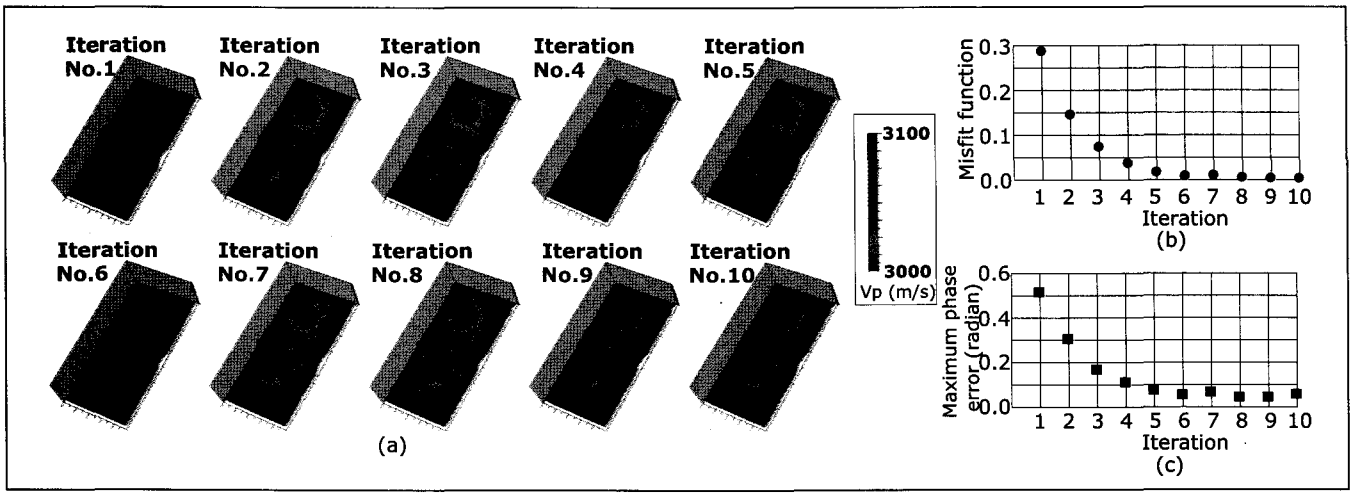

Fig. 6. Inversion processes within a single-frequency loop. (a) Inversion results obtained by the 150 Hz single-frequency inversion, using the 100 Hz loop result as an initial velocity model. (b) Misfit function. (c) Maximum phase error.

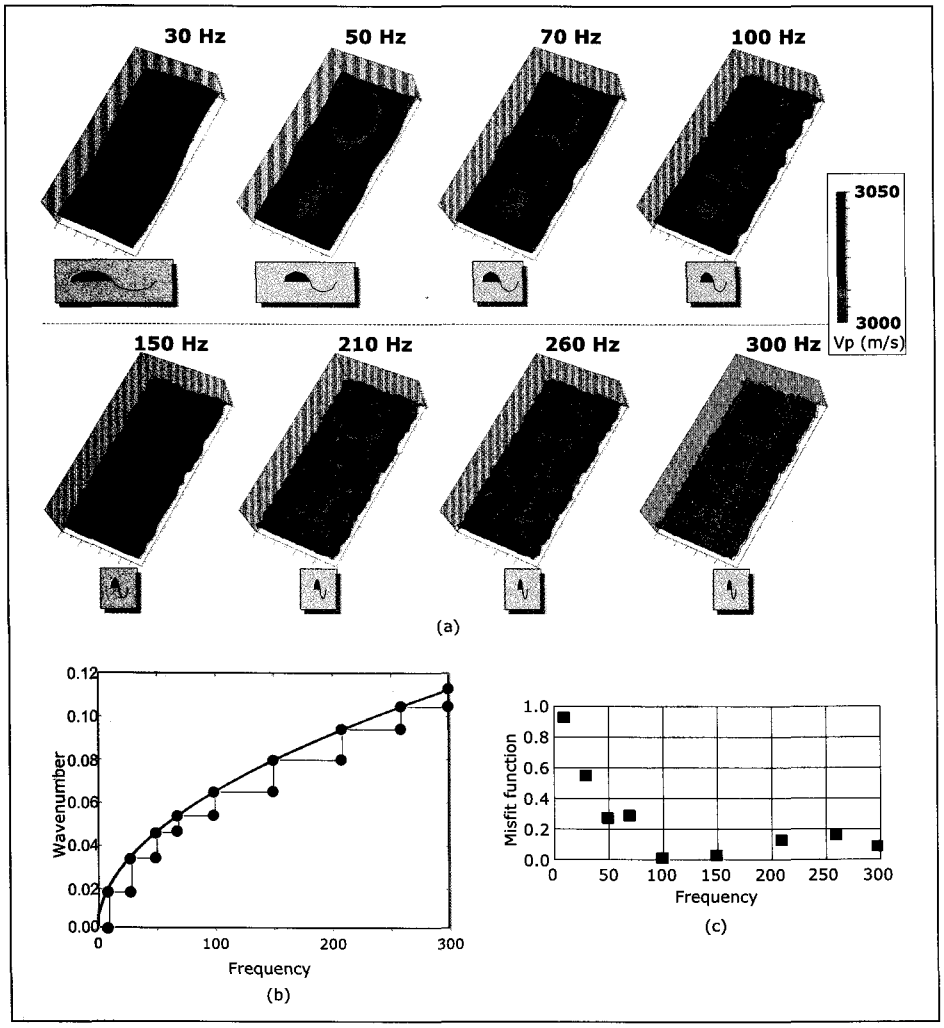

Fig. 7. Inversion results obtained with optimal frequency selection. (a) Reconstructed velocity images, with the typical wavelength, for each frequency component. (b) Scheme for optimum frequency selection. (c) Misfit functions calculated after each individual single-frequency loop.

100-Hz loop. Figures 6b and 6c show the evaluation function and the maximum phase error, respectively. Judging from the monotonically decreasing features of the two misfit indicators, it is reasonable to conclude that the single-frequency loop converges with sufficient stability.

Figure 7 shows the results of inversion obtained from the set of optimal frequencies (Figure 7b) determined by our proposed method. Figure 7a illustrates the results after individual single-frequency loops. The typical wavelength for each frequency component is also shown, below the corresponding velocity model. Figure 7c shows the evaluation function using all frequency components used for inversion, calculated by an additional forward modelling after the inversion process. Judging from Figure 7c, the series of frequencies was appropriately chosen, and the inversion has converged stably. The additional higher frequency components in the inversion have also resolved smaller anomalies, as expected. As shown in Figure 7a, the smallest anomaly (3 m diameter) was successfully reconstructed using 300 Hz ($\lambda = 10$ m) wave components. Only nine frequencies were used to reconstruct the structure shown in Figure 7a, indicating that the waveform inversion in the frequency-space domain is more efficient than that in the time-space domain, because 1024 time-samples for the time-space domain inversion is mathematically equivalent to 512 frequencies for the frequency-space domain inversion.

DISCUSSION

Figure 8 shows a case of coarser sampling in frequency space. After a single-frequency loop of f_a, we can draw a maximum phase error curve as indicated by a green line in Figure 8a. According to the method derived in this paper, we should select a frequency component used for the next mono-frequency loop to be equal to or less than f_b in order to maintain wavenumber continuity. If one sets the next frequency (f_c) above this ($f_c > f_b$), a discontinuity in wavenumber arises that gives rise to problems.

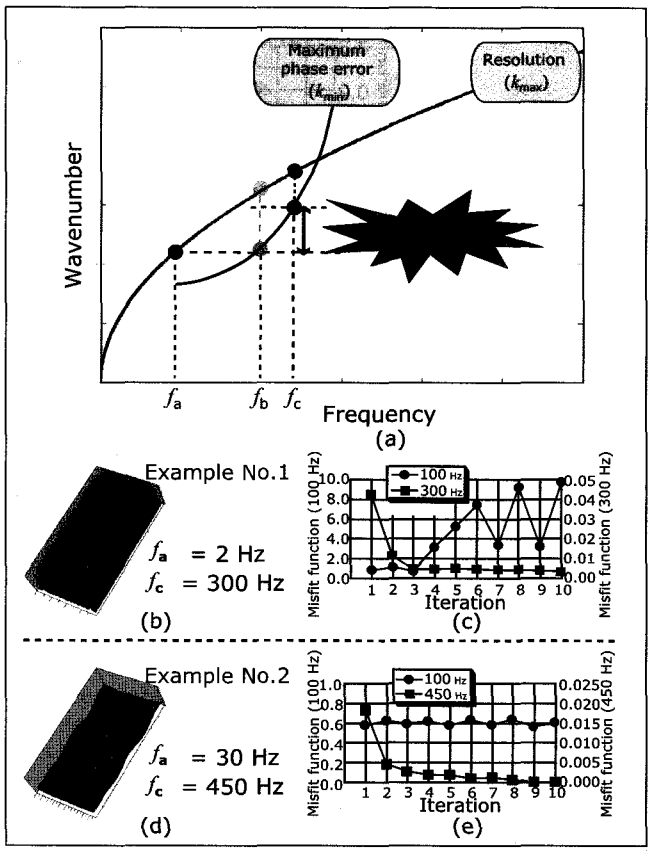

Fig. 8. Inversion result obtained without optimal frequency selection. (a) Scheme of frequency selection. (b): Reconstructed tomogram (example 1). (c) Misfit functions for example. 1. (d) Reconstructed tomogram (example 2). (e) Misfit functions of example 2.

Two examples of coarser frequency sampling are shown here. In the first example, f_a = 2 Hz, f_b = 10 Hz, and f_c = 300 Hz. Figure 8b shows the velocity model derived from this choice, and Figure 8c illustrates the misfits for the 100-Hz and 300-Hz frequencies. In the second example, f_a = 30 Hz, f_b = 50 Hz, and f_c = 450 Hz. Figures 8d and 8e show the reconstructed velocity model and misfits for individual frequencies. It is obvious that these arbitrary frequency-selection strategies fail to invert to the correct velocity model.

Figure 8c clearly indicates that the misfit of the 300-Hz frequency component decreases with every iteration. Conversely, the misfit at the peak frequency (100 Hz) rapidly increases after 3 iterations, suggesting that inversion failed due to divergence. In the second example, the misfit of the frequency used for the inversion (450 Hz) also decreases. However, only a small velocity update occurs, and the 100-Hz misfit does not vary appreciably. Consequently, the velocity model obtained is quite similar to the initial model. These examples of failed inversion demonstrate the importance of maintaining the continuity of the spatial wavenumber when selecting the frequency the next single-frequency inversion.

CONCLUSIONS

We have presented an effective strategy for selecting a set of optimal temporal frequency components for frequency-space domain waveform inversion, based on the idea of maintaining continuity of spatial wavenumbers. Determination of the frequency components to maintain wavenumber continuity between two successive single-frequency inversion loops leads to continuity of the size of the geological structure reconstructed by the inversion. That is to say, the set of optimal frequencies always satisfies the weak scattering assumptions, and it gives rise to stable inversion processes, maintaining a monotonic reduction in the misfit function during iterations.

In the inversion of a simple three-scatterer model, only nine frequencies were required to resolve the target, in contrast to the 1024 time samples required theoretically for equivalent time-domain inversion. Inversion in the frequency domain with appropriate selection of frequency samples is therefore more computationally efficient than inversion in the time domain.

Future work should focus on more realistic cases, such as extension to a three-dimensional elastic implementation, development of effective methods for estimating source wavelets from acquired data, and evaluation of the effects of noise.

ACKNOWLEDGEMENTS

The authors express their gratitude to Dr. Osamu Nishizawa of the Geological Survey of Japan, Agency of Industrial Science and Technology, and Dr. Toshiki Watanabe of the Graduate School of Environmental Studies, Nagoya University, for valuable discussions and advice. They also express their thanks to Dr. Lindsay Thomas for substantial improvement of this paper.

REFERENCES

Devaney, A.J., 1984, Geophysical diffraction tomography: *IEEE Transactions on Geoscience and Remote Sensing*, **GE-22**, 3–13.

Furumura, T., Kennett, B.L.N., and Takanaka, H., 1998, Parallel 3-D pseudospectral simulation of seismic wave propagation: *Geophysics*, **63**, 279–288.

Harris, J.M., Nolen-Hoeksema, R.C., Langan, R.T., Van Schaack, M., Lazaratos, S.K., and Rector III, J.W., 1995, High-resolution crosswell imaging of a west Texas carbonate reservoir: Part 1 - Project summary and interpretation: *Geophysics*, **60**, 667–681.

Lazaratos, S.K., and Marion, B. P., 1997, Crosswell seismic imaging of reservoir changes caused by CO2 injection: *Leading Edge*, **16**, 1300–1306.

Mathisen, M.E., Cunningham, P., Shaw, J., Vassilou, A.A., Justice, J.H., and Guinzy, N.J., 1995, Crosswell seismic radial survey tomograms and the 3-D interpretation of a heavy oil steamflood: *Geophysics*, **60**, 651–659.

Murayama, Y., Ashida, Y., and Sassa, K., 1991, Simulation of seismic disturbances by use of the Fourier transform: Theory and calculation method: *Butsuri-Tansa (Geophys. Explor.)*, **44**, 18–26 (in Japanese with English abstract).

Pratt, R.G., and Worthington, M.H., 1990, Inverse theory applied to multi-source cross-hole tomography. Part 1: Acoustic wave-equation method: *Geophysical Prospecting*, **38**, 287–310.

Pratt, R.G., Shin, C., and Hicks, G.J., 1998, Gauss-Newton and full Newton method in frequency-space seismic waveform inversion: *Geophys. J. Int.*, **133**, 341–362.

Pratt, R.G., 1999, Seismic waveform inversion in the frequency domain, part 1: Theory and verification in a physical scale model: *Geophysics*, **64**, 888–901.

Shin, C., and Sohn, H., 1998, A frequency-space 2-D scalar wave extrapolator using extended 25-point finite-difference operator: *Geophysics*, **63**, 289–296.

Shuster, G.T., 1995, Fracture resolution limits for crosswell migration and traveltime tomography: Theory: Proceedings of the 3rd SEGJ/SEG International Symposium, 86–93.

Tarantola, A., 1984, Inversion of seismic reflection data in the acoustic approximation: *Geophysics*, **49**, 1259–1266.

Tarantola, A., 1986, A strategy for nonlinear elastic inversion of seismic reflection data: *Geophysics*, **51**, 1893–1903.

Williamson, P.R., 1991, A Guide to the limits of resolution imposed by scattering in ray tomography: *Geophysics*, **56**, 202–207.

Williamson, P.R., and Worthington, M.H., 1993, Resolution limits in ray tomography due to wave behavior: Numerical experiments: *Geophysics*, **58**, 727–735.

Wong, J., 2000, Crosshole seismic imaging for sulfide orebody delineation near Sudbury, Ontario, Canada: *Geophysics*, **65**, 1900–1907.

Wu, R.S., and Toksöz, M.N., 1987, Diffraction tomography and multi-source holography, applied to seismic imaging: *Geophysics*, **52**,11–25.